ACS OMEGA

http://pubs.acs.org/journal/acsodf
Article

Linear Support Vector Machine Model of an IR Spectral Library: Application to Skin Cancer

Rebecca C. Bradley, Justin D. Erwin, Tatiana Oberyszyn, Kathleen L. Tober, Charles L. Hitchcock, Heather C. Allen, and James V. Coe*

Cite This: https://doi.org/10.1021/acsomega.5c10854
Read Online

ABSTRACT: The primary result of this work is the derivation and measurement of the average "Decision Contribution Spectrum" using a mouse tumor sample data set and the linear support vector machine (SVM) method from a perspective of spectroscopy. The "Decision Contribution Spectrum" gives the average contribution to the decision (tumor/nontumor in this case) at each step along the spectrum. A library of more than four thousand infrared (IR) spectra was obtained with a Fourier Transform Infrared (FTIR) microscope imaging system on a frozen section of an SKH1 mouse tumor - an accepted murine model for studying squamous cell carcinoma in that it very closely recapitulates the human disease. A linear SVM model was trained and tested avoiding overtraining and offering simple feature selection. It was used to see how much data can be removed without affecting the quality of decisions. Then, two further efforts are described to move IR spectroscopy toward future use in human skin cancer detection: (i) the design of a reduced range and reduced sampling for a fast and hand-held, mid-infrared spectral probe, and (ii) the use of a fiber-loop sensor probe (with FTIR in this preliminary study) on live SKH1 mice that had tumors to detect cancer externally and show no ill effects on the mice. The combination of the latter efforts supports the feasibility of using a fiber-loop sensor with a fast and hand-held mid-infrared spectral probe for the detection of skin cancer on humans. This work does not demonstrate a working human skin cancer probe, rather it provides evidence for judging whether work on live human skin is justified.

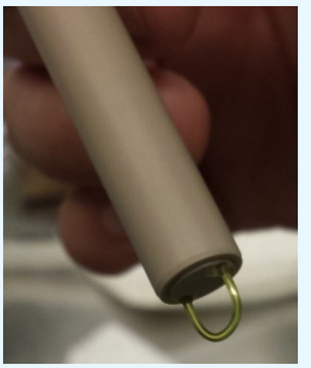

1. INTRODUCTION

Spectral libraries and machine learning methods[1] offer opportunities to extract spectral knowledge and classify unknown samples. This work features binary tumor/nontumor decisions from spectra. The most important scientific contribution of this work is the development of a linear support vector machine method from the perspective of spectroscopy, i.e., the linear support vector machine (SVM) equations from Cortes and Vapnik[2] have been rewritten in terms of scaled spectra and used to derive the "decision contribution spectrum" giving the average contribution to the decision at each wavenumber step in the spectrum, i.e., each spectral step. This work also describes how the output of only three spectra and a constant allows the use of the decision equation without the training data, which is a great benefit when training is time-consuming or compared to methods requiring on-site training. Machine learning techniques and support vector machine methods are gaining wide attention for vibrational spectroscopy in physical chemistry[3−7] and biomedical applications.[8−12] Here we show the utility of linear SVM[13−17] decision equations for spectroscopic feature analysis while also avoiding overtraining.

This work starts by deriving the "decision contribution spectrum" and making the first measurement of it in the context of mouse tumors. Then, the results are used to make progress toward the ultimate goal of a probe for human skin cancer. This work does not demonstrate the ultimate goal, rather we take the current positive results as a necessary but insufficient condition. We are judging whether work on live human skin is justified. There were three parts to this study: (1) Fourier transform infrared (FTIR) microscope imaging was recorded on a frozen section of an SKH1 mouse tumor yielding a library of 4064 IR spectra (2553 tumor spectra and 1511 nontumor). The efficacy of the linear SVM model was determined by training on half the data and testing with the other half. The "decision contribution spectrum" was then extracted to get the average contribution to the tumor/nontumor decision at each spectral step. (2) Data was removed (reduced ranges and tolerable increases in spectral step) to explore how much spectral data can be removed without adversely affecting decisions. The ranges studied started with H-stretching region vs the fingerprint region and ended with popular quantum cascade laser (QCL) ranges. (3) Finally, IR

Received: October 16, 2025
Revised: November 21, 2025
Accepted: December 3, 2025

spectra were recorded on live SKH1 mice that had tumors induced by UV irradiation using an FTIR fiber optic adapter and a fiber-loop sensor probe. The results were examined for the ability to distinguish tumors on live skin with reduced spectral range and reduced sampling within the range.

The motivating question for this work is: Can direct infrared (IR) absorption spectra, as obtained by touching live human skin with a probe, detect skin cancer on a time scale useful during a visit to the doctor's office? Mid-IR vibrational spectroscopy has long been known to be able to detect cancer[8,11,18−29] without the need for labels such as fluorophores, radiolabels, and monoclonal antibodies,[10,30] and work on diagnostic methods provides a growing foundation.[10,23,31−35] Fourier Transform Infrared (FTIR) spectroscopy,[36] a traditional IR method, has been previously utilized for the detection of skin cancer,[37,38] but current designs are too slow for fast and inexpensive diagnostic work in a doctor's office. However, tunable IR lasers are increasingly available such as the quantum cascade laser (QCL),[21,39−43] yet of greatly reduced range of tunability (compared to FTIR) while multiple QCL systems are too expensive. Future devices might employ a QCL for skin cancer[41] as has been explored for glucose detection.[44−46] The work presented here uses FTIR data to design operational features of a fast QCL mid-IR spectral probe. The work is directed toward the design only, and the working probe is left for a future paper.

2. SVM DECISION EQUATIONS WITH SPECTRAL LIBRARIES

The set of tissue spectra recorded for an experiment can be used as a library of predictors and the corresponding pathology assessments provide the response variables for training machine learning decision equations. The model used in this work is the supervised machine learning model called a Support Vector Machine (SVM) of Cortes and Vapnik,[2] which provides an optimal hypersurface for separating measurements of two classes (such as tumor and nontumor) by fitting the hypersurface to selected data called "support vectors" from the Predictor subset of spectra which lie between the two identified classes. Note that when using full IR spectra as the data set, support vectors have the form of full-range, digital IR spectra. A linear kernel function with spectral scaling minimizes overfitting and provides simplicity and feature selection, i.e., transfers best to future tests—at least for this skin cancer data set. The linear SVM decision equation value (d_k) from the Cristianini and Shawe-Taylor text[17] can be re-expressed for a full IR test spectrum ($\mathrm{Test}_{k,j}$) as

$$d_k = b + \sum_i \alpha_i y_i \left\langle \frac{\mathrm{SV}_{i,j} - \overline{\mathrm{Train}_j}}{\sigma_{\mathrm{Train}_j}} \middle| \frac{\mathrm{Test}_{k,j} - \overline{\mathrm{Train}_j}}{\sigma_{\mathrm{Train}_j}} \right\rangle \tag{1}$$

where the index i is for support vectors, j for spectral steps (the dot product index), and k for the spectrum to be tested. Furthermore, b is the scalar bias constant, α_i are the weights of the support vectors ($\mathrm{SV}_{i,j}$) chosen as spectra near the separating hypersurface, and y_i are the group membership [class 1 (tumor) and class 2 (nontumor) of the binary decision]. Since scaling is essential, the mean training spectrum ($\overline{\mathrm{Train}_j}$) is subtracted from spectra (both support vectors and the test spectra) with stepwise division of the result by the standard deviation of the training set ($\sigma_{\mathrm{Train}_j}$). The expression within the dot product brackets is called the "kernel" which allows generalization to nonlinear models, but this work uses only the linear option. Mathematically, d_k is the perpendicular distance from the separating hyperplane to a test spectrum as a decision data point. To clarify, d_k has the form of distance, but there is a component for every step in the full IR spectrum, so it is a distance with 1626 components in this case, i.e., a hyper dimensional distance. Values of $d_k > 0$ classify into one class (such as tumor), and $d_k < 0$ classify into the other (such as nontumor). In order to use the decision equations in this form, the spectral data file of every support vector needs to be transmitted to the potential user and there can easily be hundreds or thousands of support vectors—each a full IR spectrum in this example.

Since many popular machine learning models produced overtrained spectral results on this data set (high training accuracy, low accuracy on new predictions or a failure to generalize), a linear SVM model[13,17,47−49] was chosen to represent these results (the "fitcsvm" function of the MATLAB programming environment from MathWorks.com). A more useable SVM form for spectroscopists is attained by moving the support vector summation of eq 1 into the vector inner product bracket and commuting the row and column of the inner product. The decision equation is rewritten as

$$d_k = b + \left\langle \frac{\mathrm{Test}_{k,j} - \overline{\mathrm{Train}_j}}{\sigma_{\mathrm{Train}_j}} \middle| \beta_j \right\rangle,$$
$$\text{where } \beta_j = \sum_i \alpha_i y_i \left(\frac{\mathrm{SV}_{i,j} - \overline{\mathrm{Train}_j}}{\sigma_{\mathrm{Train}_j}} \right) \tag{2}$$

where β_j (the "fitcsvm.m" variable name) has the form of an IR spectrum when using the full set of spectral steps for training. The bracket at left indicates an inner dot product over spectral steps. The SVM program essentially determines optimized values for the bias offset b and β_j.In our opinion, the linear SVM result seems to be more closely related to a least-squares fit than popular machine learning models like deep neural networks. We call β_j the "SVM β spectrum". Once obtained, the decision equation itself can be extracted (by outputting three spectra and a constant, i.e., $\overline{\mathrm{Train}_j}$, $\sigma_{\mathrm{Train}_j}$, β_j, and b) and used independently of the programming environment to classify new spectra. Notice that the SVM β spectrum has contributions from all support vectors at each spectral step (see the right-side of eq 2), but such contributions have been separated-out of the left-side of eq 2. The multiplication of β_j by a scaled spectrum reveals the wavelengths that are most important in a specific decision regarding the chosen classes.

It is interesting to consider eq 2 in terms of the average class 1 ("T" for tumor) or class 2 ("NT" for nontumor) spectra, i.e. $\overline{\mathrm{T}_j}$ and $\overline{\mathrm{NT}_j}$, respectively. The average decision equation value results can be written in terms of the individual spectral steps for tumor and nontumor as

$$\overline{\mathrm{dNT}_j} = b + \sum_{j=1}^{j_{\max}} \left(\frac{\overline{\mathrm{NT}_j} - \overline{\mathrm{Train}_j}}{\sigma_{\mathrm{Train}_j}} \right) \beta_j$$
$$\text{and } \overline{\mathrm{dT}_j} = b + \sum_{j=1}^{j_{\max}} \left(\frac{\overline{\mathrm{T}_j} - \overline{\mathrm{Train}_j}}{\sigma_{\mathrm{Train}_j}} \right) \beta_j \tag{3}$$

https://doi.org/10.1021/acsomega.5c10854
ACS Omega XXXX, XXX, XXX−XXX

where j_{max} is the number of spectral steps. Examination of the difference between $\overline{dT_j}$ and $\overline{dNT_j}$ at each spectral step gives the average "Decision Contribution Spectrum"

$$\overline{\Delta d_j} = \overline{dT_j} - \overline{dNT_j} = \left(\frac{\overline{T_j} - \overline{NT_j} - \overline{Train_j}}{\sigma_{Train_j}} \right) \beta_j \quad (4)$$

at each spectral step j. The quantity $\overline{\Delta d_j}$ is determined by the average difference between tumor and nontumor spectra as scaled by the training set and multiplied by β_j, the "SVM beta" spectrum. Also note that each step of β_j corresponds to the summed contribution of all support vectors at that spectral step. An examination of $\overline{\Delta d_j}$ across the spectrum identifies the importance of spectral steps (wavenumbers in this case) which is useful if one needs to reduce the number of wavelengths employed in measuring a spectrum. This can be used for feature selection in an average sense, i.e., the selection of the most important wavenumbers on average. Conversely, it indicates that measurements are not needed at all wavenumbers, so some measurements need not be made. It is useful to begin to learn about noise in the average "decision contribution spectrum". How important are big changes in the IR spectral bands upon becoming cancerous vs contributions of the SVM beta spectrum itself? Which vibrational bands are most important to decisions? This formalism enables such questions to be investigated.

3. EXPERIMENTAL SECTION

Keratinocytic carcinoma (including basal cell and squamous cell carcinoma) is the most prevalent form of any cancer in humans.[50] The SKH1 mouse model of UV-induced cutaneous squamous cell carcinoma (SCC) is an accepted murine model for studying SCC development as it recapitulates the human disease,[51−53] so the detection of SKH1 mouse tumors serves as a good pretest for eventual use in humans for skin cancer. The animal protocol was designed to minimize pain or discomfort to the mice. All procedures were approved and performed in accordance with the University PHS Welfare Assurance number (A3261−01) and our Animal Care and Use Committee (IACUC protocol 2010A00000083, approved 2/4/16). An SKH-1 mouse developed tumors after exposure to UV, three-times daily, for 14 weeks. One tumor was obtained for a frozen section using FTIR microscope imaging and live mice with tumors were probed with a fiber-loop sensor and FTIR fiber optic adapter.

3.1. FTIR Microscope Imaging of a Frozen Section. Full-range IR spectra were recorded on a frozen section of an SKH1 mouse tumor using hyperspectral microimaging with a PerkinElmer Spotlight 400 Fourier Transform Infrared (FTIR) instrument as shown in Figure 1. Details of acquiring a ∼3 μm thick frozen section of an SKH1 mouse tumor are given in Supporting Information (see Figure S1). The red rectangle (1.588 mm × 0.100 mm area) in Figure 1 of the frozen section was imaged with 254 × 16 = 4064 square pixels each with 6.25 μm square edges. An FTIR spectrum was recorded at each pixel (4000−750 cm^{-1} spectral range, 4 cm^{-1} resolution, 2 cm^{-1} steps, 16 scans per pixel taking ∼90 min, with a liquid N_2-cooled MCT detector). Afterward, the exact same tissue in the same sample holder was stained with H&E[54] and imaged with a different optical microscope. The result has been overlaid in registry with the yellowish pre-IR imaging picture

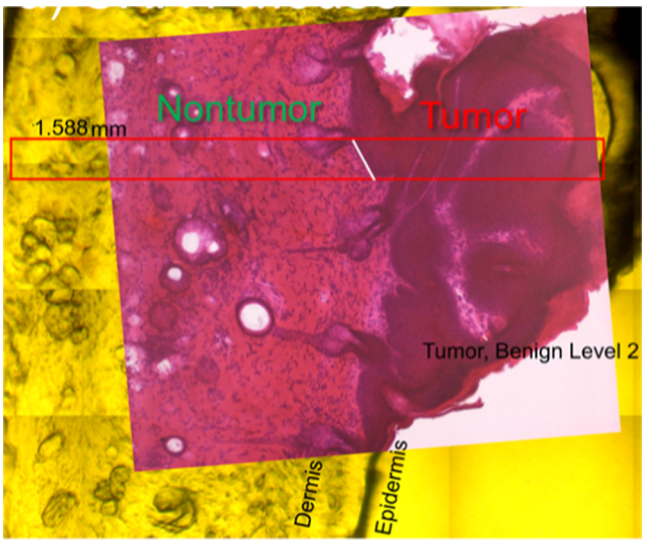

Figure 1. An unstained frozen section of ∼ 3 μm of thickness was positioned on a ZnSe IR window (yellow underneath image) for examination under an IR microscope. The red rectangle indicates a region that was subjected to microscopic IR hyperspectral imaging. Afterward, an H&E stain (top reddish overlay) was obtained of the exact same tissue and imaged under an optical microscope. The two images were scaled, oriented, and overlaid in registry. Epidermis (skin exterior) is to the right, dermis (skin interior) is to the left. The tumor (right) stained dark red, while the nontumor (left) was much lighter. A white line shows the separation between tumor and nontumor to establish the response variables. Note that the dermis side of the dermis/epidermis interface was punctuated with hair follicles (vertically down the center).

by means of scaling and a slight counterclockwise rotation. Note that the H&E image had a ZnSe yellow color cast which was removed and then contrast-adjusted using Adobe Photoshop Elements 2.0 ("Enhance" tab, "Adjust Color" option, and "Color Cast"). The epidermis stained dark red with H&E, as did the tumor. Pixels to the right of the white line were indexed as tumor class, while pixels to the left were indexed as nontumor class for use as response variables for machine learning routines. The clear delineation between tumor and nontumor regions made for an ideal data set for fitting an SVM β spectrum, group decision equations, and feature selection.

3.2. Live Mouse Spectra. A fiber optic coupler (Harrick FiberMate 2) was placed in the sample region of a PerkinElmer Spectrum 100 FTIR (Figure 2a) and connected to an ATR fiber-loop probe sensor[55,56] (Art Photonics, Figure 2b). Mid-IR radiation flows through the fiber-loop sensor (zoom in Figure 2c) including a component that travels a few wavelengths outside of the loop as an evanescent wave before heading back to the spectrometer's detector. After a background spectrum is recorded with the fiber-loop in air, then the fiber-loop is touched to skin (see Supporting Information and Figure S2) which absorbs IR from the evanescent wave due to the vibrational bands of tissue proteins, lipids, and other biomolecules yielding a sample spectrum. The negative log of the ratio of the spectrum signal (touching skin) to the background (air) gives an absorption spectrum of skin tissue. Fiber optics limited the useable range of the PerkinElmer Spectrum 100 FTIR to 1800−700 cm^{-1} (the FTIR instrument is typically 4000−700 cm^{-1}) and spectra were recorded on and off tumors using 25 scan averages, 1 cm^{-1} steps, 4 cm^{-1}

https://doi.org/10.1021/acsomega.5c10854
ACS Omega XXXX, XXX, XXX−XXX

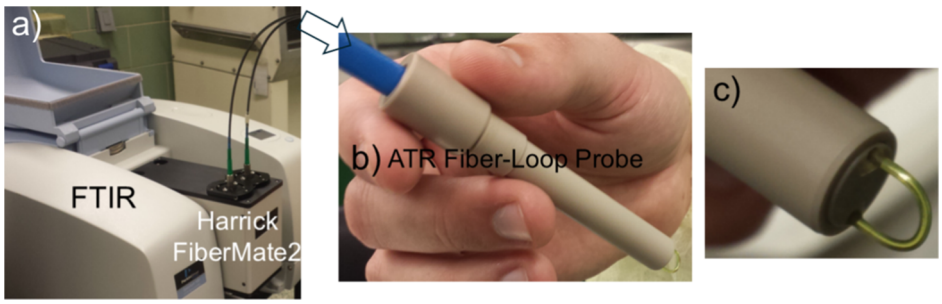

Figure 2. (a) Fiber optic coupler (Harrick FiberMate2) is placed in the sample compartment of a PerkinElmer Spectrum 100 FTIR. (b) An Art Photonics fiber-loop ATR probe sensor is coupled to the FTIR with mid-IR fiber optics. (c) Zoomed image of the fiber-loop sensor through which IR light travels from and back to the FTIR. The IR includes an evanescent component traveling a few wavelengths outside of the loop allowing spectra to be recorded of things that the probe touches.

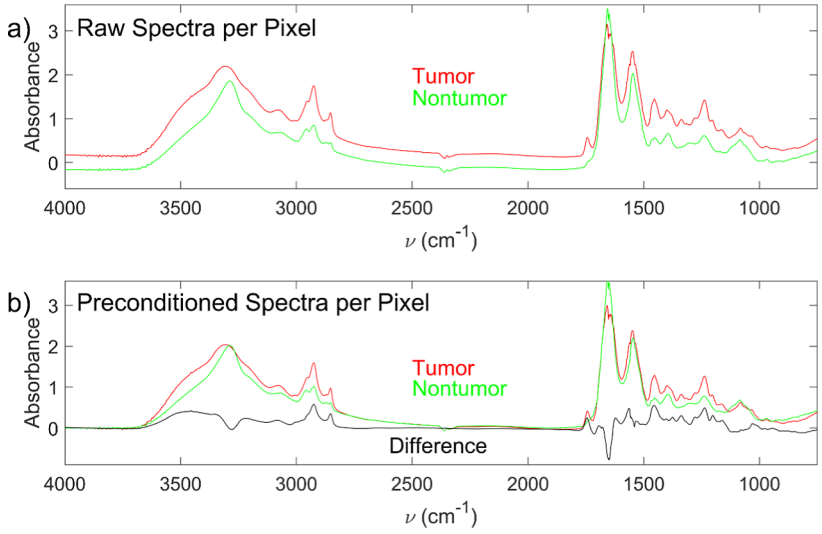

Figure 3. (a) Raw average tumor (red) and nontumor (green) spectra of an SKH1 mouse frozen section. (b) Since the baselines were quite different, a baseline correction was applied before machine learning analysis. The tumor and nontumor difference (black trace) shows significant differences between the tumor and nontumor spectra.

resolution, with a liquid N_2-cooled MCT detector, requiring about 2.5 min each. The tumors had thick keratinized tops so that the probe could not push into the tumor as it could for normal skin, so these spectra had much less intensity because a smaller surface area of the fiber-loop probe touched sample. Note that tumors are often stiffer than normal tissue.[57,58] We obtained 16 nontumor and 12 tumor spectra for analysis.

4. RESULTS

4.1. FTIR of SKH1 Tumor Frozen Section Results. The tissue section had a clearly indicated transition from tumor to nontumor (white line in Figure 1) which was used to define the response variables. There were 2553 tumor spectra and 1511 nontumor spectra for a total of 4064 full-range spectra—each corresponding to a 6.25 μm × 6.25 μm pixel. Figure 3a shows the average raw IR spectra of the tumor (red) and nontumor (green) regions on a per pixel basis. The SKH1 mouse tumor shows an average increase in lipid CH_2 fat chains (2924 cm^{-1} and 2852 cm^{-1}, matching spectra of monooleate and lard) as has been seen in some other cancers.[59,60] It is interesting that the class baselines (probably due to scattering) were so different. Consequently, the spectra were preconditioned with a baseline correction as shown in Figure 3b. The absolute intensities are meaningful (as they are on a per pixel basis—unlike the live mouse spectra) and there are definitive differences between the tumor and nontumor regions as highlighted by the black trace in Figure 3b which is the average difference spectrum. As a first test, the set of 4064 spectra were randomly divided into two groups with ∼half for training and the remainder for testing. A linear SVM routine (MATLAB's "fitcsvm" function with scaling "Standardize" option) was trained on one-half and tested with the other. Histograms of the decision equation values [d_k, see eq 2] from three successive random partitions are overlaid for training in Figure 4a and for testing in Figure 4b. The nontumor results are plotted with green and the tumor results in red. Notice that there is no overlap between green and red for the trainings, so there are no errors in any of the trainings. Upon testing, notice a very small amount of overlap corresponding to small errors (0.34% in one run). A 10-fold cross validation was done using the 50% training results showing an error of 0.35 ± 0.41%. The histograms provide visual evidence of an excellent model (of course it is only one tissue sample).

The average contribution to the tumor/nontumor decision at each spectral step j, $\overline{\Delta d}_j$, is given in Figure 5 (blue trace) using the full spectral library of baseline corrected spectra. Extended sections labeled "Noise" with blue arrows have little difference in the tumor and nontumor spectra due to the lack of fundamental vibrations in these regions. They contribute

https://doi.org/10.1021/acsomega.5c10854
ACS Omega XXXX, XXX, XXX−XXX

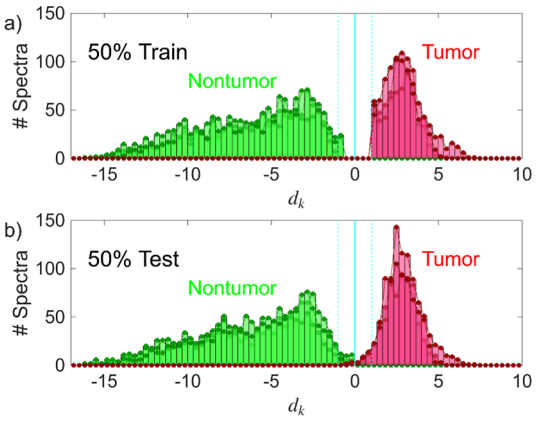

Figure 4. (a) The linear SVM decision equation value histograms of three random training runs (random ∼50% of the spectra) are overlaid with true tumor (red) and true nontumor (green). The cyan line is the decision equation dividing line and the dotted cyan lines correspond to ± a standard deviation of the scaled support vectors. There are no training errors as illustrated by no overlap of the green and red distributions. (b) The corresponding testing for each of three runs shows a small amount of overlap which averages to an error of 0.35%, i.e. accuracy is 99.65%.

much noise to the tumor decision and might be profitably eliminated from the machine learning input. The important signals are in the H-stretch and fingerprint regions. Prominent peaks in the Decision Contribution Spectrum are labeled with vertical labels in cm^{-1} in Figure 5. In the fingerprint region, there are strong negative features at 1106, 1120, 1646, 1656, and 1714 cm^{-1} and strong positive features at 938, 1018, 1162, 1344, 1456, 1540, and 1736 cm^{-1}. In the H-stretch region, there are strong negative peaks at 3102, 3128, and 3300 cm^{-1} and strong positive ones at 2930, 3314, and a broad positive range from 3314 to 3642 cm^{-1}. These must be considered relative to the absorption bands in the FTIR spectra, but they often do not occur at the absorption band maxima. The largest integrated feature is the negative peak at 1120 cm^{-1} extending from 1044 to 1142 cm^{-1} which corresponds to a region with the PO_2 symmetric stretch of many phosphorylated molecules (∼1083 cm^{-1}) and C−O bands of carbohydrates like glycogen (1008 cm^{-1}). The most intriguing feature is the sharp negative peak at 1714 cm^{-1} extending from 1702 to 1732 cm^{-1} which is in the region of ester-linked lipids (∼1741 cm^{-1}). Finally, there is much positive and negative structure in the amide I and II band regions suggesting protein band shape changes upon becoming cancerous. There does not seem to be one peak that dominates the decision; and all the bands in the H-stretch and fingerprint regions make contributions to the tumor decision, so in theory "the more, the better". However, practical probe design considerations might favor one region over another. Which regions are best?

4.2. Identifying Probe Ranges and Spectral Steps for Spectral Devices. The regions 3670−2790 cm^{-1} (Region 1) or 1860−760 cm^{-1} (Region 2) of Figure 5 are good for decisions because they correspond to fundamental vibrational bands of biomolecules.[10,61] Region 1 is the H stretching region (OH, NH, and CH stretches) with strong protein bands (amide A and B) and lipid bands (C−H stretches of CH_2 chains and CH_3), while Region 2 is sometimes called the "fingerprint" region which has lipid, amide I and II, phosphate, glycogen bands and many other biomolecules. If FTIR was too slow and complex (moving optical parts, liquid nitrogen detectors), then a QCL might be employed for a medical device with the disadvantage of a limited spectral range. So, which range is better for a limited range spectral device? Mittal and Bhargava[62] addressed this issue with breast tissues and found only small differences with "the fingerprint region-based classifiers consistently emerging as more accurate." Region 2 seems to have strong and sharp changes in $\overline{\Delta d_j}$ (see Figure 5) at the amide I and II bands and a big downward feature near phosphate and glycogen bands. Note that regions with some wavenumbers good for tumor decisions and others for nontumor are likely best for cancer decisions. The linear SVM calculations were repeated using only spectral data from each region, i.e. removing all data not in the specified range. Region 1 gave a training error of 0.27% (full data set was 0%) and had a 10-fold cross-validation error of 0.54 ± 0.34%. Region 2 gave a training error of 0% (same as full range set) and a 10-fold cross-validation error of 0.10 ± 0.17%. Again, like Mittal and Bhargava,[62] the fingerprint region is found to be more accurate.

QCLs are available in the fingerprint region (Region 2), but not the OH, NH, and CH stretch region (Region 1). Consider that they frequently have only 200 cm^{-1} tuning ranges, although larger ranges are possible.[63] So, a program using linear SVM was written to calculate the accuracy using only a 200 cm^{-1} range of data and then that range was scanned across

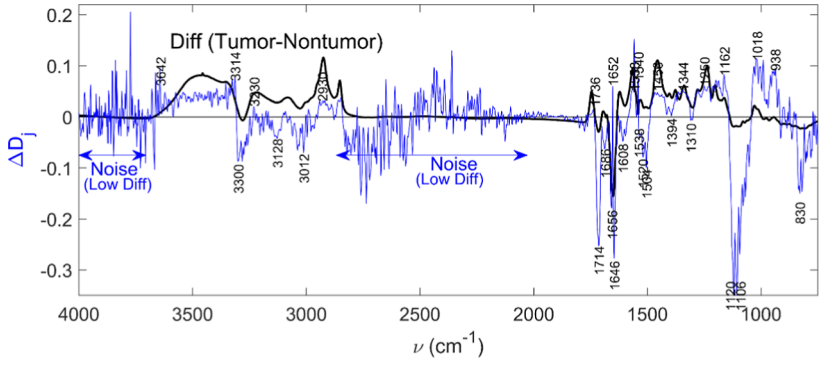

Figure 5. Average contribution to the tumor/nontumor decision (blue trace) at each spectral step j for the SKH1 mouse frozen section. The black trace is the difference between the averaged and preconditioned spectra of tumor and nontumor. The regions label "Noise" are regions where there is little difference in spectra as there are no fundamental vibrations of biomolecules in these regions. The regions from 1860 to 760 cm^{-1} and 3670−2790 cm^{-1} show important positive and negative contributions to the tumor decision.

https://doi.org/10.1021/acsomega.5c10854
ACS Omega XXXX, XXX, XXX−XXX

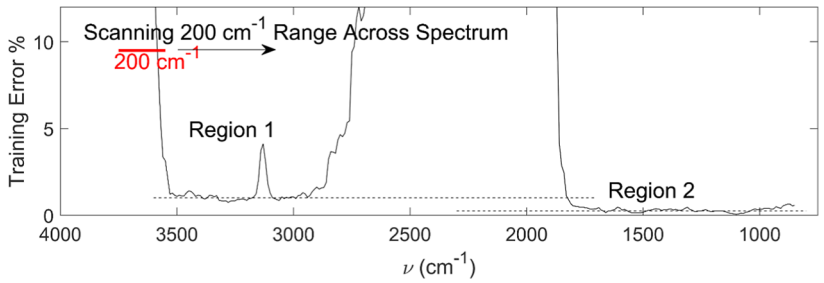

Figure 6. Training error using only a 200 cm^{-1} range (red) of the full set as that range is tuned across the spectrum. The smallest errors are in Regions 1 and 2, but the errors in Region 2 (fingerprint region) are smaller than Region 1.

the spectrum. The training error results are shown in Figure 6. Again, like Mittal and Bhargava,[62] limited ranges in the fingerprint region are found to be more accurate—although both regions are useable.

Which of the four common single QCL ranges (that are often configured to work as one unit in IR microscopes[42]) is best for skin cancer work? The ranges 1850−1644 cm^{-1}, 1642−1352 cm^{-1}, 1350−986 cm^{-1}, and 984−780 cm^{-1} were investigated by using only data from each spectral step (2 cm^{-1} intervals) in these regions to obtain decisions. The Training errors and 10-fold cross-validation errors are given in Supporting Information (Table S1). The second (amide band region) and third region had the lowest errors, i.e., 10-fold cross-validation errors of 0.30 ± 0.30% and 0.05 ± 0.16%, respectively. More importantly, it is clear that one need not make measurements at each spectral step. Calculations were done using every other step (4 cm^{-1} intervals), every fifth step (10 cm^{-1} intervals), and every 10th step (20 cm^{-1} intervals). There is roughly a doubling of error when only every 10th step is used (90% of the data are dropped) vs use of all data. Details are in Supporting Information, Table S1. As an example, a QCL operating from 1350 to 986 cm^{-1} could measure at 37 wavelengths in 10 cm^{-1} steps obtaining a result as good as the full spectrum training. Therefore, in addition to reducing the range for a spectral cancer probe, one can also reduce the number of wavenumbers measured. In fact, 9 out of 10 measurements were dropped in analysis without significantly degrading decisions.

4.3. Spectral Evaluation of Live Tissue. The above results involved scanning tumor directly, now consider a situation closer to our desired application—namely probing the skin of a living entity. Raw spectra of living mice are shown in Figure 7 in which all the nontumor spectra were of higher absorbance intensity. Examination of the raw spectra in Figure 7 shows that there is perfect separation of tumor and nontumor spectra based on the absolute intensity of the spectra. However, this is not useful as the probe can be pushed into tissue differently—by different investigators or on different occasions by the same investigator. Spectral preprocessing was guided by the previous imaging work and involved subtracting the baseline average in the region from 1800 to 1770 cm^{-1} and normalizing the result to control for different probe pressure and tissue elasticity as shown in Figure 8a. The averages of the preconditioned spectra are given in Figure 8b showing significant differences (black trace) in spite of normalization. Finally, a linear SVM decision equation was trained with the 28 preconditioned spectra, and the corresponding histogram of the decision equation values is given in Figure 8c showing zero errors upon training. One can still discriminate tumor and nontumor on live skin even if the tumor elasticity hint is removed by normalization and the decision equations are different than that for frozen sections.

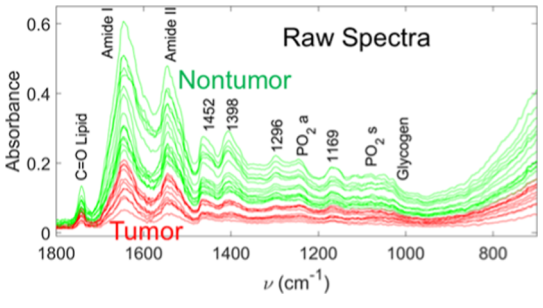

Figure 7. Raw probe FTIR spectra at the base of tumors (red) and off tumors (nontumor, green).

The average contribution to the tumor/nontumor decision at each spectral step [$\overline{\Delta d}_j$ of eq 4] is plotted in Figure 9 with blue. The sharpness of the features was surprising with widths of ∼4 cm^{-1} matching the FTIR resolution. The most intense features are in the amide I and II band regions although there is a concentration of smaller features in the 1130−950 cm^{-1} region of glycogen and phosphorylated biomolecules. This type of feature analysis suggests that a probe for live skin might work best in the amide I and II band region. Also, one might not need to measure signals where $\overline{\Delta d}_j$ is close to zero which means that spectra could be more quickly recorded by only measuring wavenumbers labeling the maxima and minima of $\overline{\Delta d}_j$ or at large and equal steps across the region.

5. CONCLUSIONS

The large FTIR microscope imaging spectral data set (2553 full-range tumor spectra and 1511 full-range nontumor spectra) of the frozen section of the SKH1 hairless mouse tumor showed significant differences between the average tumor and nontumor spectra—even after baseline correction. The absolute intensities are meaningful as all spectra correspond to the same pixel area and tissue thickness, however the desire for use in more applications led to preconditioning with baseline correction and normalization. The data were analyzed with a linear SVM model which both avoids overtraining and offers simple feature selection of the "decision contribution spectrum". Training randomly on ∼50% and testing on the remainder (∼50%) gave zero training errors and small testing errors (0.34% in one run). A 10-fold cross validation on the full library using the 50% training gave error of 0.35 ± 0.41%. The errors of cross-validation and testing were small and similar, suggesting that linear SVM gave good

https://doi.org/10.1021/acsomega.5c10854
ACS Omega XXXX, XXX, XXX−XXX

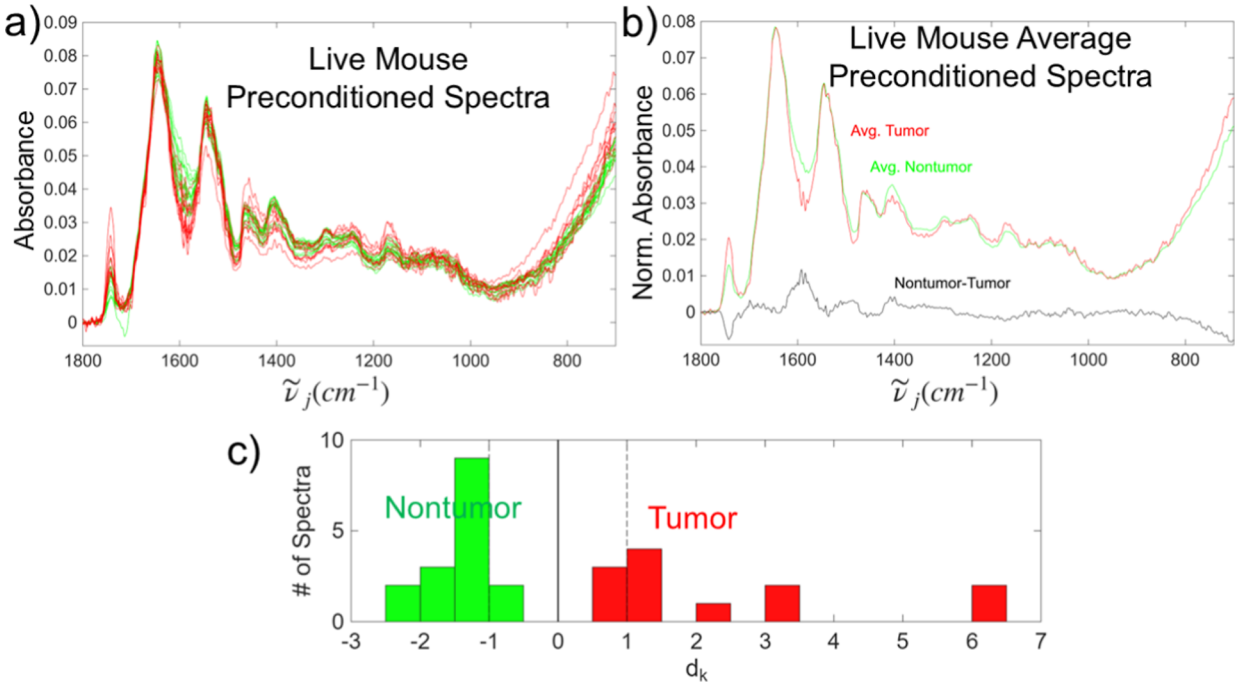

Figure 8. (a) The 12 tumor (red) and 16 nontumor (green) spectra after preconditioning with a baseline correction and normalization, i.e. no clear separation. (b) The average tumor (red) and nontumor (green) spectra after preconditioning in which the black trace is the difference between the average nontumor and tumor spectra showing significant changes. (c) Histogram of the linear SVM decision equation values showing zero mistakes in spite of preconditioning.

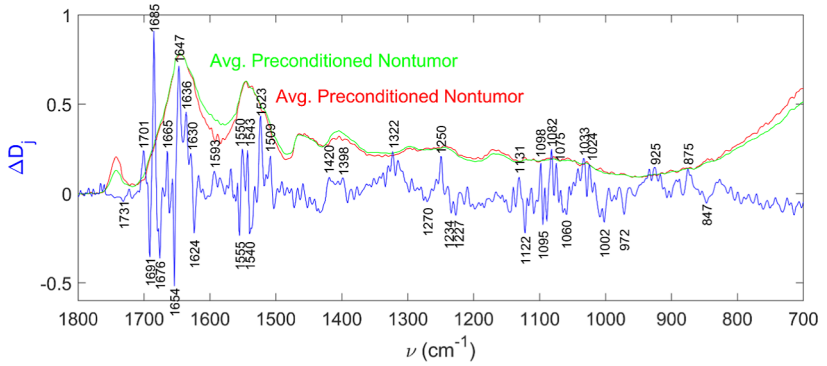

Figure 9. Average contribution to the tumor/nontumor decision (blue trace) at each spectral step j for the SKH1 mouse frozen section. Many maxima and minima are labeled in units of cm^{-1}. The average preconditioned spectra of tumor (red) and nontumor (green) are plotted for reference. The largest contributions to tumor decisions seem to come from the amide I and II band regions.

decision equations. The average Decision Contribution Spectrum regarding the tumor/nontumor decision [$\overline{\Delta d_j}$ of eq 4] is given in Figure 5. There is noise in ranges devoid of vibrational bands. The largest integrated feature in the Decision Contribution Spectrum comes as a negative peak at 1120 cm^{-1} corresponding to the PO_2 symmetric stretch of many phosphorylated molecules, carbohydrates and/or polysaccharides. There is a sharp negative peak at 1714 cm^{-1} with rapid changes in intensity which is in the region of ester-linked lipids (~1741 cm^{-1}). There is also much positive and negative structure in the amide I and II band regions suggesting protein band shape changes upon becoming cancerous. There does not seem to be one peak that dominates the decision; and all the bands in the H-stretch and fingerprint regions make contributions to the tumor decision.

Given good training and testing results, the effects of removing data were examined. Two spectral regions had sharp positive and negative features with rapidly changing trends that indicate where fundamental vibrations in tissue change upon becoming cancerous. Region 1 was the H stretching region (3670−2790 cm^{-1}, amide A and B, lipid CH_2 chains and CH_3) and Region 2 was the "fingerprint" region (1860−760 cm^{-1}, lipid, amide I and II, phosphate, glycogen bands and many other biomolecules). Both regions can discriminate tumor from nontumor, but Region 2, the fingerprint region, does so with more accuracy (Figure 6). The fingerprint region was further divided into subregions commonly covered by popular commercial QCL systems. Such systems can be integrated, i.e. programing or tuning like one broadly tunable laser, but they are expensive. Considering that a device for medical practice might only be able to have one QCL, four subregions were tested, and each was found to do a decent job at discriminating tumor. The subregion from 1350 to 986 cm^{-1} was most accurate. Then, each subregion was studied as spectral steps

https://doi.org/10.1021/acsomega.5c10854
ACS Omega XXXX, XXX, XXX−XXX

were dropped revealing only a doubling of the error rate even after removing 90% of the data. This implies that practical mid-IR spectral probes can be designed with just one QCL (a very reduced range compared to FTIR) and that the device might measure with 10 or 20 cm^{-1} steps or sampling intervals (at a higher resolution than FTIR) allowing fast and decisive spectra to be recorded on live human skin.

Finally, spectra were recorded on the outer skin of live mice. In this part of the study, 16 nontumor and 12 tumor spectra from live SKH1 hairless mice were recorded in the region from 1800 to 700 cm^{-1} and there was excellent separation of tumor and nontumor spectra based on the absolute intensity. Preconditioned spectra were successfully trained with linear SVM which made no training errors in distinguishing tumor. The average Decision Contribution Spectrum of Figure 9 reveals the most critical wavenumbers in the protein and lipid region for live skin assay. It identifies critical wavenumbers that should and need not be measured. Since the mid-IR fiber optics filtered away the OH, NH, and CH stretching region, this work shows that a reduced range in the fingerprint region compared to that of traditional full-range FTIR can be viable in distinguishing cancer. Of course, the frozen section work already revealed greatly reduced ranges and increased sampling intervals that look promising. These results show that it is possible to detect skin cancer externally and with no ill effects on the living entities. The current positive results are necessary but insufficient conditions for demonstration of the ultimate goal of probing live human skin. We conclude that the combination of a fiber-loop sensor with a fast mid-infrared spectral probe (of reduced range and increased sampling interval relative to FTIR) is worthy of examination for live human skin. Clinical trials of this device are warranted on skin cancer in humans.

■ ASSOCIATED CONTENT

Supporting Information

The Supporting Information is available free of charge at https://pubs.acs.org/doi/10.1021/acsomega.5c10854.

A PDF file with figures and description are provided for the mouse frozen section, anesthesia and live mouse probing, and a table of errors upon removing spectral data (PDF)

■ AUTHOR INFORMATION

Corresponding Author

James V. Coe − *Department of Chemistry and Biochemistry, The Ohio State University, Columbus, Ohio 43210-1173, United States;* Present Address: Emeritus Faculty at The Ohio State University.; orcid.org/0000-0001-5009-5472; Email: coe.1@osu.edu

Authors

Rebecca C. Bradley − *Department of Chemistry and Biochemistry, The Ohio State University, Columbus, Ohio 43210-1173, United States; IR Medtek LLC, Gahanna, Ohio 43230, United States*

Justin D. Erwin − *Department of Chemistry and Biochemistry, The Ohio State University, Columbus, Ohio 43210-1173, United States*

Tatiana Oberyszyn − *Department of Pathology, The Ohio State University, Columbus, Ohio 43210, United States;* Present Address: Vice Dean for Faculty Affairs and Professor of Pathology, The Ohio State University College of Medicine

Kathleen L. Tober − *Department of Pathology, The Ohio State University, Columbus, Ohio 43210, United States;* Present Address: Director, Faculty Affairs Operations at The Ohio State University, College of Medicine.; orcid.org/0000-0001-6201-6989

Charles L. Hitchcock − *Department of Pathology, The Ohio State University, Columbus, Ohio 43210, United States;* Present Address: Emeritus Faculty at The Ohio State University.

Heather C. Allen − *Department of Chemistry and Biochemistry, The Ohio State University, Columbus, Ohio 43210-1173, United States;* orcid.org/0000-0003-3120-6784

Complete contact information is available at: https://pubs.acs.org/10.1021/acsomega.5c10854

Notes

The authors declare no competing financial interest.

■ ACKNOWLEDGMENTS

We thank The Ohio State University TCO Accelerator Award (Ohio State grant number CHE 1800414) and IR Medtek LLC (Ohio State grant number GR117057) for support.

■ REFERENCES

(1) Ferguson, A. L.; Hachmann, J.; Miller, T. F.; Pfaendtner, J. The Journal of Physical Chemistry A/B/C Virtual Special Issue on Machine Learning in Physical Chemistry. *J. Phys. Chem. B* **2020**, *124* (44), 9767−9772.

(2) Cortes, C.; Vapnik, V. Support-vector networks. *Mach. Learn.* **1995**, *20* (3), 273−297.

(3) Maksudov, F.; Jones, L. K.; Barsegov, V. Statistical Learning from Single-Molecule Experiments: Support Vector Machines and Expectation−Maximization Approaches to Understanding Protein Unfolding Data. *J. Phys. Chem. B* **2021**, *125* (22), 5794−5808.

(4) Chen, B.; Lu, Y.; Pan, W.; Xiong, J.; Yang, Z.; Yan, W.; Liu, L.; Qu, J. Support Vector Machine Classification of Nonmelanoma Skin Lesions Based on Fluorescence Lifetime Imaging Microscopy. *Anal. Chem.* **2019**, *91* (16), 10640−10647.

(5) Ito, K.; Ogawa, Y.; Yokota, K.; Matsumura, S.; Minamisawa, T.; Suga, K.; Shiba, K.; Kimura, Y.; Hirano-Iwata, A.; Takamura, Y.; et al. Host Cell Prediction of Exosomes Using Morphological Features on Solid Surfaces Analyzed by Machine Learning. *J. Phys. Chem. B* **2018**, *122* (23), 6224−6235.

(6) Li, H.; Liang, Y.; Xu, Q. Support vector machines and its applications in chemistry. *Chemometr. Intell. Lab. Syst.* **2009**, *95* (2), 188−198.

(7) Liu, H.; Yao, X.; Zhang, R.; Liu, M.; Hu, Z.; Fan, B. Accurate Quantitative Structure−Property Relationship Model To Predict the Solubility of C60 in Various Solvents Based on a Novel Approach Using a Least-Squares Support Vector Machine. *J. Phys. Chem. B* **2005**, *109* (43), 20565−20571.

(8) Lasch, P.; Petrich, W. Data acquisition and analysis in biomedical vibrational spectroscopy. *RSC Analytical Spectroscopy Series*; The Royal Society of Chemistry, 2010; pp 192−225.

(9) Lasch, P.; Stammler, M.; Zhang, M.; Baranska, M.; Bosch, A.; Majzner, K. FT-IR hyperspectral imaging and artificial neural network analysis for identification of pathogenic bacteria. *Anal. Chem.* **2018**, *90* (15), 8896−8904.

(10) Baker, M. J.; Trevisan, J.; Bassan, P.; Bhargava, R.; Butler, H. J.; Dorling, K. M.; Fielden, P. R.; Fogarty, S. W.; Fullwood, N. J.; Heys, K. A.; et al. Using Fourier transform IR spectroscopy to analyze biological materials. *Nat. Protoc.* **2014**, *9* (8), 1771−1791.

https://doi.org/10.1021/acsomega.5c10854
ACS Omega XXXX, XXX, XXX−XXX

(11) Lasch, P.; Haensch, W.; Naumann, D.; Diem, M. Imaging of colorectal adenocarcinoma using FT-IR microspectroscopy and cluster analysis. *Biochim. Biophys. Acta, Mol. Basis Dis.* **2004**, *1688* (2), 176−186.
(12) Naumann, D. FT-infrared and FT-Raman spectroscopy in biomedical research. *Appl. Spectrosc. Rev.* **2001**, *36* (2−3), 239−298.
(13) Li, Q. B.; Wang, W.; Ling, X. F.; Wu, J. G. Detection of Gastric Cancer with Fourier Transform Infrared Spectroscopy and Support Vector Machine Classification. *Biomed. Res. Int.* **2013**, *2013*, 942427.
(14) Bergner, N.; Romeike, B. F. M.; Reichart, R.; Kalff, R.; Krafft, C.; Popp, J. U. Tumor Margin Identification and Prediction of the Primary Tumor from Brain Metastases using FTIR Imaging and Support Vector Machines. *Analyst* **2013**, *138* (14), 3983−3990.
(15) Widjaja, E.; Zheng, W.; Huang, Z. W. Classification of Colonic Tissues Using Near-Infrared Raman Spectroscopy and Support Vector Machines. *Int. J. Oncol.* **2008**, *32* (3), 653−662.
(16) Schölkopf, B.; Smola, A. J. *Learning with Kernels: Support Vector Machines, Regularization, Optimization, and Beyond*; MIT Press, 2002.
(17) Cristianini, N.; Shawe-Taylor, J. *An Introduction to Support Vector Machines and Other Kernel-based Learning Methods*; Cambridge University Press, 2000.
(18) Chiriboga, L.; Diem, M.; Lee, H. Analysis of liver using FT-IR microscopy. *FASEB J.* **2000**, *14* (4), A701.
(19) Chiriboga, L.; Xie, P.; Yee, H.; Zarou, D.; Zakim, D.; Diem, M. Infrared spectroscopy of human tissue. IV. Detection of dysplastic and neoplastic changes of human cervical tissue via infrared microscopy. *Cell. Mol. Biol.* **1998**, *44* (1), 219−229.
(20) Fabian, H.; Thi, N. A. N.; Eiden, M.; Lasch, P.; Schmitt, J.; Naumann, D. Diagnosing benign and malignant lesions in breast tissue sections by using IR-microspectroscopy. *Biochim. Biophys. Acta Biomembr.* **2006**, *1758* (7), 874−882.
(21) Bhargava, R. Infrared spectroscopic imaging: the next generation. *Appl. Spectrosc.* **2012**, *66* (10), 1091−1120.
(22) Fernandez, D. C.; Bhargava, R.; Hewitt, S. M.; Levin, I. W. Infrared spectroscopic imaging for histopathologic recognition. *Nat. Biotechnol.* **2005**, *23* (4), 469.
(23) Mackanos, M. A.; Contag, C. H. Fiber-Optic Probes Enable Cancer Detection with FTIR Spectroscopy. *Trends Biotechnol.* **2010**, *28* (6), 317−323.
(24) Spielvogel, J.; Lobik, L.; Nissencorn, I.; Hibst, R.; Gotshal, Y.; Katzir, A. Cancer diagnostics using Fourier transform fiber optic infrared evanescent wave spectroscopy (FTIR-FEWS). *Proc. SPIE* **1998**, *3262*, 185−191.
(25) Fabian, H.; Lasch, P.; Boese, M.; Haensch, W. Mid-IR microspectroscopic imaging of breast tumor tissue sections. *Biopolymers* **2002**, *67* (4−5), 354−357.
(26) Fabian, H.; Lasch, P.; Boese, M.; Haensch, W. Infrared microspectroscopic imaging of benign breast tumor tissue sections. *J. Mol. Struct.* **2003**, *661*, 411−417.
(27) Coe, J. V.; Chen, Z.; Li, R.; Nystrom, S. V.; Butke, R.; Miller, B.; Hitchcock, C. L.; Allen, H. C.; Povoski, S. P.; Martin, E. W., Jr. Molecular constituents of colorectal cancer metastatic to the liver by imaging infrared spectroscopy. *Proceedings SPIE 9328 (Imaging, Manipulation, and Analysis of Biomolecules, Cells, and Tissues XIII)*; SPIE, 2015; Vol. *93280*.
(28) Coe, J. V.; Chen, Z.; Li, R.; Butke, R.; Miller, B.; Hitchcock, C. L.; Allen, H. C.; Povoski, S. P.; Martin, E. W., Jr. Imaging infrared spectroscopy for fixation-free liver tumor detection *Proceedings SPIE 8947 Imaging, Manipulation, and Analysis of Biomolecules, Cells, and Tissues XII*; SPIE, 2014..*8947*
(29) Chen, Z.; Butke, R.; Miller, B.; Hitchcock, C. L.; Allen, H. C.; Povoski, S. P.; Martin, E. W.; Coe, J. V. Infrared Metrics for Fixation-Free Liver Tumor Detection. *J. Phys. Chem. B* **2013**, *117* (41), 12442−12450.
(30) Walsh, M. J.; Reddy, R. K.; Bhargava, R. Label-Free Biomedical Imaging With Mid-IR Spectroscopy. *IEEE J. Sel. Top. Quantum Electron.* **2012**, *18* (4), 1502−1513.
(31) Bhargava, R. Towards a practical Fourier transform infrared chemical imaging protocol for cancer histopathology. *Anal. Bioanal. Chem.* **2007**, *389* (4), 1155−1169.
(32) Litjens, G.; Sánchez, C. I.; Timofeeva, N.; Hermsen, M.; Nagtegaal, I.; Kovacs, I.; Hulsbergen-van de Kaa, C.; Bult, P.; van Ginneken, B.; van der Laak, J. Deep learning as a tool for increased accuracy and efficiency of histopathological diagnosis. *Sci. Rep.* **2016**, *6*, 26286.
(33) Hibler, B. P.; Qi, Q.; Rossi, A. M. Current state of imaging in dermatology. *Semin. Cutan. Med. Surg.* **2016**, *35* (1), 2−8.
(34) Tiwari, S.; Bhargava, R. Extracting knowledge from chemical imaging data using computational algorithms for digital cancer diagnosis. *Yale J. Biol. Med.* **2015**, *88* (2), 131−143.
(35) Sattlecker, M.; Stone, N.; Bessant, C. Current trends in machine-learning methods applied to spectroscopic cancer diagnosis. *TrAC, Trends Anal. Chem.* **2014**, *59*, 17−25.
(36) Al-Kelani, M.; Buthelezi, N. Advancements in medical research: Exploring Fourier Transform Infrared (FTIR) spectroscopy for tissue, cell, and hair sample analysis. *Skin Res. Technol.* **2024**, *30* (6), No. e13733.
(37) Kyriakidou, M.; Anastassopoulou, J.; Tsakiris, A.; Koui, M.; Theophanides, T. FT-IR Spectroscopy Study in Early Diagnosis of Skin Cancer. *In Vivo* **2017**, *31* (6), 1131.
(38) Basov, S.; Dankner, Y.; Weinstein, M.; Katzir, A.; Platkov, M. Technical Note: Noninvasive mid-IR fiber-optic evanescent wave spectroscopy (FEWS) for early detection of skin cancers. *Med. Phys.* **2020**, *47* (11), 5523−5530.
(39) Yeh, K.; Kenkel, S.; Liu, J.-N.; Bhargava, R. Fast Infrared Chemical Imaging with a Quantum Cascade Laser. *Anal. Chem. (Washington, DC, U.S.)* **2015**, *87* (1), 485−493.
(40) Bird, B.; Baker, M. J. Quantum Cascade Lasers in Biomedical Infrared Imaging. *Trends Biotechnol.* **2015**, *33* (10), 557−558.
(41) Charlton, C.; Katzir, A.; Mizaikoff, B. Infrared Evanescent Field Sensing with Quantum Cascade Lasers and Planar Silver Halide Waveguides. *Anal. Chem.* **2005**, *77* (14), 4398−4403.
(42) Bird, B.; Rowlette, J. A protocol for rapid, label-free histochemical imaging of fibrotic liver. *Analyst* **2017**, *142* (8), 1179−1184.
(43) Faist, J.; Capasso, F.; Sivco, D. L.; Sirtori, C.; Hutchinson, A. L.; Cho, A. Y. Quantum Cascade Laser. *Science* **1994**, *264* (5158), 553−556.
(44) Yu, S.; Li, D.; Chong, H.; Sun, C.; Yu, H.; Xu, K. In vitro glucose measurement using tunable mid-infrared laser spectroscopy combined with fiber-optic sensor. *Biomed. Opt. Express* **2014**, *5* (1), 275−286.
(45) Sasaki, R.; Kino, S.; Matsuura, Y. Mid-infrared photoacoustic spectroscopy based on ultrasound detection for blood component analysis. *Biomed. Opt. Express* **2023**, *14* (7), 3841−3852.
(46) Pleitez, M. A.; Lieblein, T.; Bauer, A.; Hertzberg, O.; von Lilienfeld-Toal, H.; Mäntele, W. In vivo noninvasive monitoring of glucose concentration in human epidermis by mid-infrared pulsed photoacoustic spectroscopy. *Anal. Chem.* **2013**, *85* (2), 1013−1020.
(47) Chen, Z. Human Liver Metastases: Chemometrics of Imaging FTIR Data. Doctoral Dissertation, The Ohio State University, 2015.
(48) Majumder, S. K.; Ghosh, N.; Gupta, P. K. Support Vector Machine for Optical Diagnosis of Cancer. *J. Biomed. Opt.* **2005**, *10* (2), 024034.
(49) Bradley, R. C. *Spectroscopy and Machine Learning: Development of Methods for Cancer Detection Using Mid-Infrared Wavelengths*. Doctoral Dissertation, The Ohio State University, 2021. http://rave.ohiolink.edu/etdc/view?acc_num=osu1620658484449199.
(50) Aggarwal, P.; Knabel, P.; Fleischer Jr, A. B. United States burden of melanoma and non-melanoma skin cancer from 1990 to 2019. *J. Am. Acad. Dermatol.* **2021**, *85* (2), 388−395.
(51) Benavides, F.; Oberyszyn, T. M.; VanBuskirk, A. M.; Reeve, V. E.; Kusewitt, D. F. The hairless mouse in skin research. *J. Dermatol. Sci.* **2009**, *53* (1), 10−18.
(52) Oberyszyn, T. M.; Sabourin, C. L. K.; Bijur, G. N.; Oberyszyn, A. S.; Boros, L. G.; Robertson, F. M. Interleukin-1α gene expression

https://doi.org/10.1021/acsomega.5c10854
ACS Omega XXXX, XXX, XXX−XXX

and localization of interleukin-1α protein during tumor promotion. *Mol. Carcinog.* **1993**, *7* (4), 238−248.
(53) Sullivan, N. J.; Tober, K. L.; Burns, E. M.; Schick, J. S.; Riggenbach, J. A.; Mace, T. A.; Bill, M. A.; Young, G. S.; Oberyszyn, T. M.; Lesinski, G. B. UV Light B-Mediated Inhibition of Skin Catalase Activity Promotes Gr-1+CD11b+ Myeloid Cell Expansion. *J. Invest. Dermatol.* **2012**, *132* (3−1), 695−702.
(54) Prophet, E. B. *Laboratory Methods in Histotechnology*; American Registry of Pathology, 1992.
(55) Sanghera, J.; Kung, F.; Pureza, P.; Nguyen, V.; Miklos, R.; Aggarwal, I. D. Infrared evanescent-absorption spectroscopy with chalcogenide glass fibers. *Appl. Opt.* **1994**, *33* (27), 6315−6322.
(56) Romanova, E. A.; Korsakova, S.; Komanec, M.; Nemecek, T.; Velmuzhov, A.; Sukhanov, M.; Shiryaev, V. S. Multimode chalcogenide fibers for evanescent wave sensing in the mid-IR. *IEEE J. Sel. Top. Quantum Electron.* **2017**, *23* (2), 289−295.
(57) Radman, B. A.; Alhameed, A. M. M.; Shu, G.; Yin, G.; Wang, M. Cellular elasticity in cancer: a review of altered biomechanical features. *J. Mater. Chem. B* **2024**, *12* (22), 5299−5324.
(58) Tilleman, T. R.; Tilleman, M. M.; Neumann, M. H. The elastic properties of cancerous skin: Poisson's ratio and Young's modulus. *Isr. Med. Assoc. J.* **2004**, *6* (2), 735.
(59) Daniëls, V. W.; Smans, K.; Royaux, I.; Chypre, M.; Swinnen, J. V.; Zaidi, N. Cancer cells differentially activate and thrive on de novo lipid synthesis pathways in a low-lipid environment. *PLoS One* **2014**, *9* (9), No. e106913.
(60) Long, J.; Zhang, C.-J.; Zhu, N.; Du, K.; Yin, Y.-F.; Tan, X.; Liao, D.-F.; Qin, L. Lipid metabolism and carcinogenesis, cancer development. *Am. J. Cancer Res.* **2018**, *8* (5), 778.
(61) Barth, A.; Zscherp, C. What vibrations tell about proteins. *Q. Rev. Biophys.* **2002**, *35* (04), 369−430.
(62) Mittal, S.; Bhargava, R. A comparison of mid-infrared spectral regions on accuracy of tissue classification. *Analyst* **2019**, *144* (8), 2635−2642.
(63) Lehtinen, J.; Kuusela, T. Broadly tunable quantum cascade laser in cantilever-enhanced photoacoustic infrared spectroscopy of solids. *Appl. Phys. B: Laser Opt.* **2014**, *115* (3), 413−418.

https://doi.org/10.1021/acsomega.5c10854
ACS Omega XXXX, XXX, XXX−XXX